Theoretical analysis and experimental verification on the static properties of externally pressurized air-bearing pads with load compensation

P.L. Holster and J.A.H. Jacobs

Load compensation can lead to externally pressurized bearings with infinite stiffness at the operating conditions. Calculations and experiments carried out on these bearings are discussed in this paper for two types of circular bearing pads with compliant surfaces. The mathematics is amply treated in appendices, and the numerical procedures are illustrated in diagrams. The experimental set-up is explained.

Keywords: *air bearings, load compensation, numerical analysis, bearing pad design*

Introduction

Today externally pressurized circular air-bearing pads are used successfully in several kinds of machines, such as grinding machines with aerostatic guideways and journals with thrust bearings. For many applications the stiffness of the bearing is an important characteristic. Although the stiffness of an aerostatic bearing is sufficient in most cases, there is a demand for bearings with still higher stiffnesses.

Infinite stiffnesses or even negative stiffnesses have proved possible by using bearings with load compensation by means of a compliant bearing surface. At the 1971 Gas Bearing Symposium Kilmister[1] presented such a bearing pad (Fig 1(a)), and at the 1974 Symposium Rowe and Kilmister[2] gave an incompressible analysis thereof. Blondeel, Snoeys and Devrieze[3] described an approximate design calculation for similar bearing pads (Fig 1(b)) at the 1976 Gas Bearing Symposium. Also, Hayashi[4] gave an investigation of such a bearing at the 1981 Symposium in which the compressibility at the inlet orifice is neglected. Our colleagues Franken and Hagen patented such a bearing (Fig 1(c)) with a pivoting membrane[5]. Recently also, Zeiss[6] applied for a patent for such a bearing. The bearing type with pivoting membrane (Fig 1(c)) only works satisfactorily at a rather high supply pressure of more than 6 bar and an outer diameter of 60 mm or more.

Our aim was to design such a bearing with the same infinite stiffness at a lower supply pressure and a smaller outer diameter. Therefore, it was necessary to investigate the influence of several parameters and to predict the load-carrying capacity versus gap height variation by means of calculations.

An additional difficulty for this kind of calculation is the flexibility of the bearing surface. The deflection of the membrane depends on the pressure distribution in the bearing gap, while that pressure distribution is influenced by the geometry of the bearing gap. The interaction of these phenomena can be dealt with numerically by solving the equations with the relaxation method.

Philips Research Laboratories, PO Box 80.000, 5600 JA Eindhoven, The Netherlands

Also the flow through the inlet restrictor must be adequately described and gives rise to other iterations.

In this paper a solution method is derived that enables us to write a Fortran program to be used by designers. Specific parts of that program are illustrated by diagrams based on the M. Jackson method[7]. Below the M. Jackson blocks

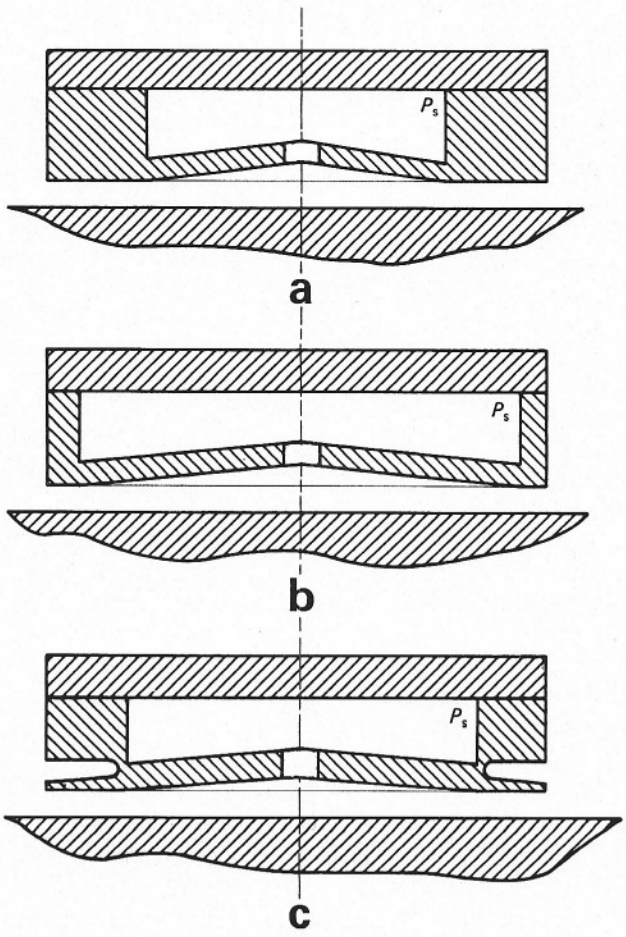

Fig 1 (a) Kilmister-type bearing pad; (b) Leuven type; (c) Philips type

 0301–679X/87/050276–14 $03.00

reference is made to other diagrams (at subroutines, indicated by double lines) or to formulae. Finally, some calculation results are compared with measurements.

General description of air bearings with a compliant surface

Bearing with a rigid non-parallel gap shape

The operation of a circular bearing pad, with a rigid non-parallel surface will be discussed briefly first. Air with a supply pressure p_s is fed through an inlet restrictor into the bearing gap. The pressure distribution in the bearing gap depends on the shape of the gap (for instance, conical). For simple gap shapes with constant conicity one can derive an analytical equation for the flow–pressure relationship. In Appendix A the algorithm for the calculation of gap flow through an arbitrary gap shape is given. The pressure drop across the restrictor depends on the compensation method. If the orifice aperture is much smaller than the annular aperture at the circumference of the orifice, the bearing is orifice-compensated. In the other case the bearing is inherently compensated.

In our case, gap heights vary from 1 μm to approximately 30 μm and orifice diameters are about 0.5 mm, so we could consider inherent compensation for the ease of calculation. To achieve better accuracy and to enlarge the applicability of the calculation results we choose to consider the orifice aperture and the inherent aperture to be arranged in series. The calculation of the flow through these two restrictors is elaborated in Appendix B.

Bearing with a pivoting membrane

A schematical design of this bearing with a pivoting membrane is shown in Fig 1(c). During fabrication the membrane can be ground flat with a certain over-pressure in the chamber. At atmospheric conditions the membrane will show a more or less conical form. It is also possible to grind the membrane conical without an over-pressure in the chamber.

A load-carrying capacity versus gap height characteristic for this bearing is shown in Fig 2. The deflection of the membrane is illustrated too. The dashed line will appear during measurements and represents the situation where the centre of the membrane touches the opposite surface, as will be obvious from point d in figure 2.

The pressure in the chamber acting upon the membrane will not vary during operation, so the variation in bending of the membrane depends only on the variation of the pressure distribution in the bearing gap. For a supply pressure higher than the grinding pressure and a low external load, the inner membrane will bend downwards. Then there is a large pressure drop across the restrictor. When the external load increases, the gap height tends to decrease and so does the air mass flow, resulting in a decreased pressure drop across the restrictor. This yields larger pressures in the gap, resulting in a higher load-carrying capacity. Moreover, the membrane is forced to a more convergent gap shape that additionally enlarges the load-carrying capacity. Owing

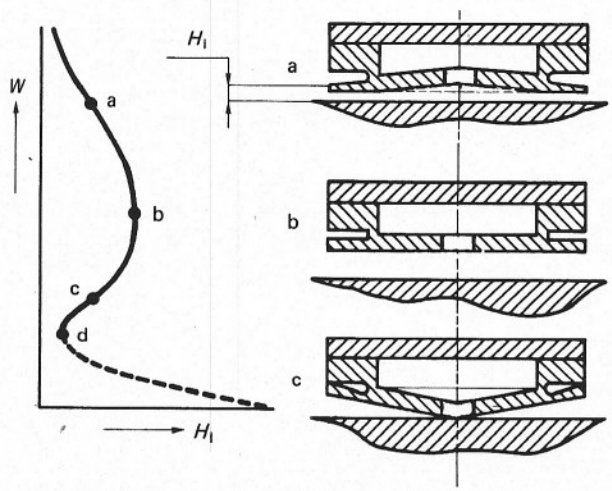

Fig 2 Typical bearing characteristics of the Philips-type bearing pad. The deflection of the membrane at positions a, b and c is drawn at the right-hand side of the figure

Notation

a	relaxation factor
C_{di}	discharge coefficient inherent aperture
C_{do}	orifice discharge coefficient
D_i	flexural rigidity inner membrane, Nm
D_o	flexural rigidity outer membrane, Nm
f	constant factor = 0.98
$H(i)$	nodal gap height, m
$H_c(i)$	calculated nodal membrane deflection, m
$H_g(i)$	nodal gap geometry, m
H_l	bearing displacement, m
H_{min}	minimum gap height, m
H_i	thickness of inner membrane, m
H_o	thickness of outer membrane, m
i	index nodal points
I_o	*DO* variable start loop
Int	see Eq (A10)
i_s	index pivot point
I_W	*DO* variable load loop
K	see Eq (B7)
M_{gap}	mass flow in the gap, kg/s
n	index outer nodal point
$P(i)$	nodal pressure, Pa
P_a	ambient pressure, Pa
$P_c(i)$	calculated $P(i)$, Pa
P_{in}	gap entrance pressure, Pa
P_{or}	orifice downstream pressure, Pa
P_s	supply pressure, Pa
P_{th}	theoretical inlet restrictor downstream pressure, Pa
$R(i)$	nodal radius, m
R_g	gas constant, J/(kg K)
R_s	pivot radius, m
T	absolute temperature, K
W	load-carrying capacity, N
W_1	W due to $P_{th} < P_{in}$, N
W_2	W due to inlet hole, N
W_c	calculated W, N
W_{max}	ultimate load, N
ΔW	step in load loop, N
ΔH	relaxation step in bearing displacement, m
η	dynamic viscosity, Pas
ν	Poisson's ratio

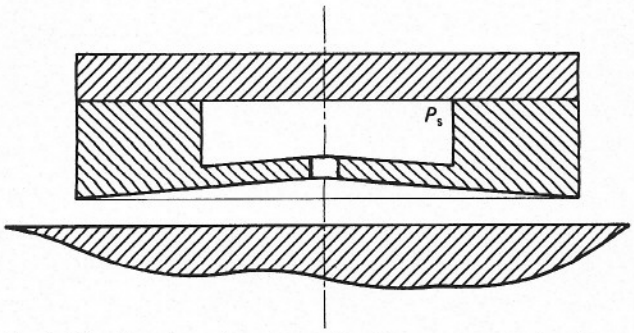

Fig 3 Kilmister-type bearing pad with a convergent outer region

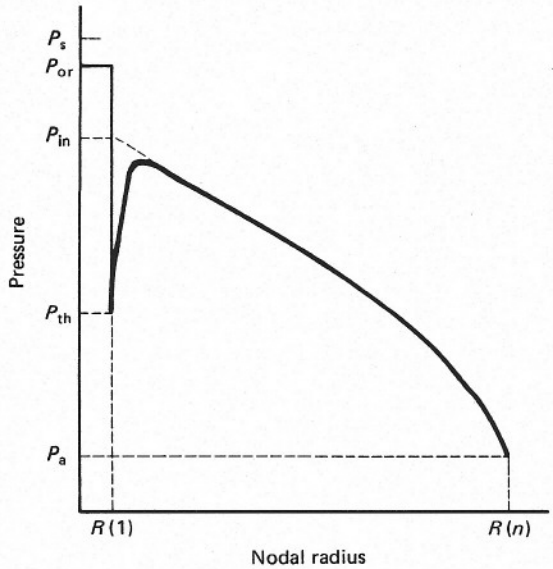

Fig 4 Pressure profile of a circular bearing pad. Through the inlet restrictor the pressure drops from supply pressure, P_s, to pressure P_{or} behind the orifice aperture, and thereafter to P_{th} after the inherent aperture. In the bearing gap a pressure recovery to P_{in} takes place

to the pivot joint the outer edge of the membrane will be bent downwards, which intensifies the effect once more. So one can imagine that the load-carrying capacity is increased without decreasing the gap height, so infinite stiffness is accomplished.

In the case of inherent compensation, the deflection of the membrane also changes the inlet aperture in an advantageous way. The latter effect on its own is capable of generating infinite stiffness.

Bearing with a clamped membrane

A schematical layout of this bearing with a clamped membrane is shown in figure 1(a). Kilmister has already proved that this type of load compensation can lead to bearings with infinite or even negative stiffness at operating conditions[1]. A small improvement is given in Fig 3 where the conical outer region will result in a higher maximum load-carrying capacity. During fabrication the bearing is ground conical with or without a certain over-pressure in the chamber.

In the same way as for the previous bearing type the inner membrane will bend inwards when the external load increases. Now the gap shape remains almost the same because of the rigid outer region. So in this bearing it is the variation of inherent inlet aperture that is mainly responsible for the gain in stiffness.

Calculation method

Pressure distribution

Since the relaxation method of calculation is used the shape of the gap is given during the calculation of the pressure profile. Because of the axisymmetry (no tilt) the calculations are one-dimensional. The gap shape is approximated by taking several nodes in the radial direction and assuming a conical gap shape between these nodes.

For isothermal compressible flow in Appendix A it is derived that for each segment between the nodes (i) and (i+1) one can express the pressure decay by (Eq (A9)):

$$P^2\ (i) - P^2\ (i{+}1) = (12\eta\, R_g\, T/\pi)\, M_{gap}\, Int\,(H\,(i),$$
$$R\,(i), H\,(i{+}1), R\,(i{+}1))$$

Because the mass flow, M_{gap}, is a constant, one can simply add all the above equations to find (see Eq (A11)):

$$P_{in}^2 - P_a^2 = (12\eta\, R_g\, T/\pi)\, M_{gap} \sum_{i=1}^{n-1} Int\,(i)$$

The ambient pressure, P_a, at the outer radius is used as boundary condition. On the other hand the pressure $P_{in} = P\,(1)$ at $R\,(1)$ is determined by equating the mass flow through the bearing gap and the mass flow through the inlet restrictor.

The flow through the inlet restriction, composed of a (fixed) orifice and an inherent aperture arranged in series, is described in Appendix B. In Fig 4 one can find the various pressures existing in the inlet restrictor. For the orifice flow (pressure drop from P_s to P_{or}) we use the compressible Bernouilli equation with a constant discharge coefficient $C_{do} = 0.8$. For the inherent aperture (with a pressure drop from P_{or} to P_{th}) we used the same equation with $C_{di} = 0.9$. But then a pressure recovery to P_{in} takes place as described by the K factor (actual pressure drop divided by theoretical pressure drop). For the value of the K factor we have used the empirical relationship as presented by McCabe, Elrod and others[8] at the 1969 Gas Bearing

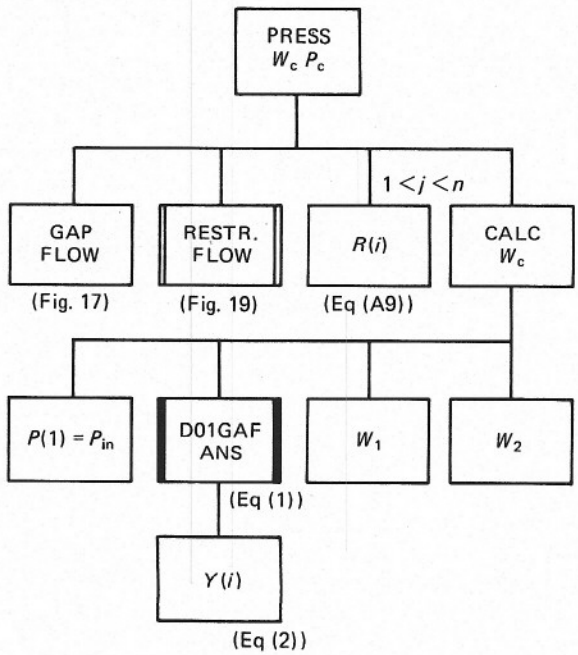

Fig 5 Diagram of the method for calculating load-carrying capacity

Symposium, where K is related to the Reynolds number only.

Load-carrying capacity

Having determined the pressure after the restrictor, P_{in}, and the mass flow through the gap, we can start to calculate the gap pressures P_c (1, . . . , n) at the nodal points R (1, . . . , n) successively. Integration of the pressure distribution over the entire surface gives the load capacity. Fig 5 illustrates the way of calculation, explained below.

For the integration we use a NAG-subroutine called DO1GAF that integrates a function, Y, which is specified numerically at nodes over the whole of its specified area. So the solution, named W, equals

$$W = \int_{R(1)}^{R(n)} Y(i)\, dR \qquad (1)$$

We choose nodes at intervals of R (n)/10 starting with R (1) at the inlet hole. An extra node R (2) at R (1)/f is chosen to imitate the pressure depression effect. The value of f can be chosen but is normally set to 0.98. Another extra node R (n-1) at $f R$ (n) assures that at very small gap heights the pressure is still adequately approximated.

The calculation of load-carrying capacity consists of three stages. First we use Eq (1) with $P(1) = P_{in}$, to avoid a sharp change in the pressure gradient, with

$$Y(i) = 2\pi R(i) P(i) \qquad (2)$$

Then a correction W_1 is performed to take the pressure depression into account, and finally the correction W_2 makes allowance for the pressure inside the inlet restrictor.

Deflection of the membrane

For a description of the deflection calculations we start with the bearing type with a pivoting membrane. On account of the axisymmetry a model of half the diameter suffices.

We start to calculate the deflections by means of the FEM package GIFTS. The mesh generated by the GIFTS pre-processor consists of axisymmetric 4-node elements, or in GIFTS terms QA4 elements[9]. The total mesh is shown in Fig 6. A simpler geometry is obtained by modelling the pivoting area by a pivot point fixed in the radial direction, as shown in Fig 7.

In Table 1 the calculated deflection at the nodes R (1) and R (n) is given for two models with the same loading case. In this loading case the inner membrane is under a pressure of 5.5 bar. Comparing the calculated values with the measured ones we see that the simpler model of Fig 7 applies equally well as the model of Fig 6.

Table 1 Comparison of FEM-calculated and measured membrane deflections at the centre, R (1), and at the periphery, R (n)

Deflection, μm		
Nodes at radius	R (1)	R (n)
Model of Fig 6	14.44	3.573
Model of Fig 7	14.88	4.185
Measured values	16.	4.0

R (n) = 30 mm, R_s = 22.9 m, H_i = 2.3 mm, H_o = 1.8 mm, P = 5.5 bar

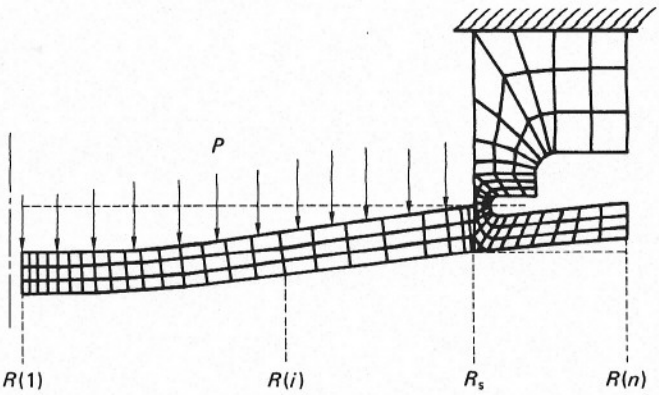

Fig 6 Mesh partition used in the FEM calculation of the deflection of the full bearing pad with pivot

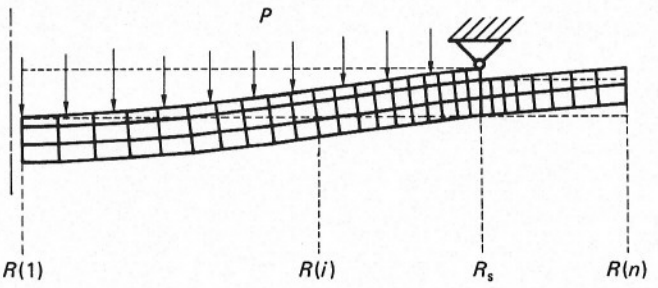

Fig 7 Mesh partition used in the FEM calculation of the deflection (Fig 6)

Encouraged by this result and to save computer time, the possibility of an analytical procedure is investigated. For these calculations the membrane is bisected into the inner part (subscript i) and the outer part (subscript o). Considering the membrane in a bent situation, the interaction between both parts is determined by the forces and moments as illustrated in Fig 25. An extra complication arises because of the different thicknesses H_i and H_o of the inner and outer membranes.

For the analytical deflection calculations the radius is divided into segments with the same nodes as used for the pressure calculation. The pressure distribution in the gap is approximated by a linear interpolation between the prescribed pressures at the nodes. In Appendices C and D the mathematics of the above procedure is given.

To check this analytical model we compare the results shown in Table 1. The same loading case for the analytical model gives a deflection of 13.4 μm at R (1) and 3.1 μm at R (n). So the analytical model corresponds as well with the measured deflections as the FEM does.

The principle of the deflection calculations for the bearing with clamped inner membrane (Fig 1) is the same. Because only one inner membrane with simple boundary conditions is involved the calculations have been somewhat simplified. A more detailed description can be found in Appendix C.

Coupling of pressure and deflection calculations

In a static situation the interaction between pressure distribution and deflection of the membrane must be in equilibrium. The usual iteration method to solve this problem is based on the so-called relaxation method. Even for very low values of the Young's modulus this method shows good convergence in our calculation.

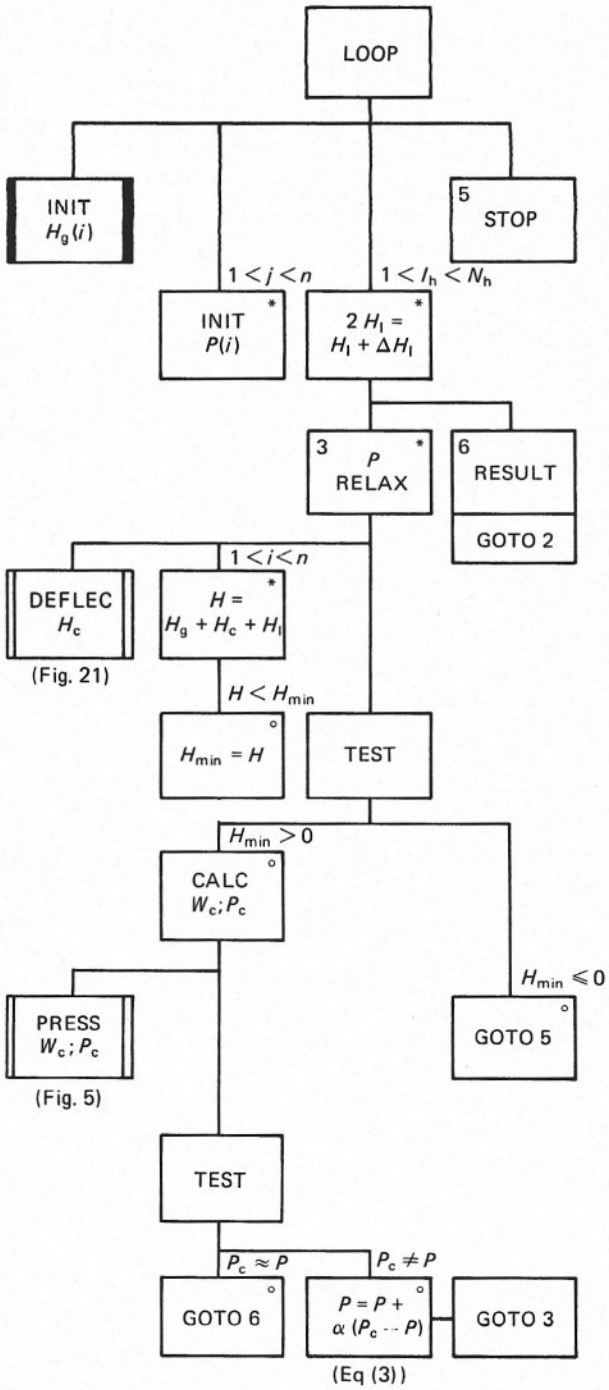

Fig 8 Simplified diagram of the calculation of load-carrying capacity, W, *at prescribed bearing displacements,* H_l. *The GOTO statements are used for clarity here but not in the actual program*

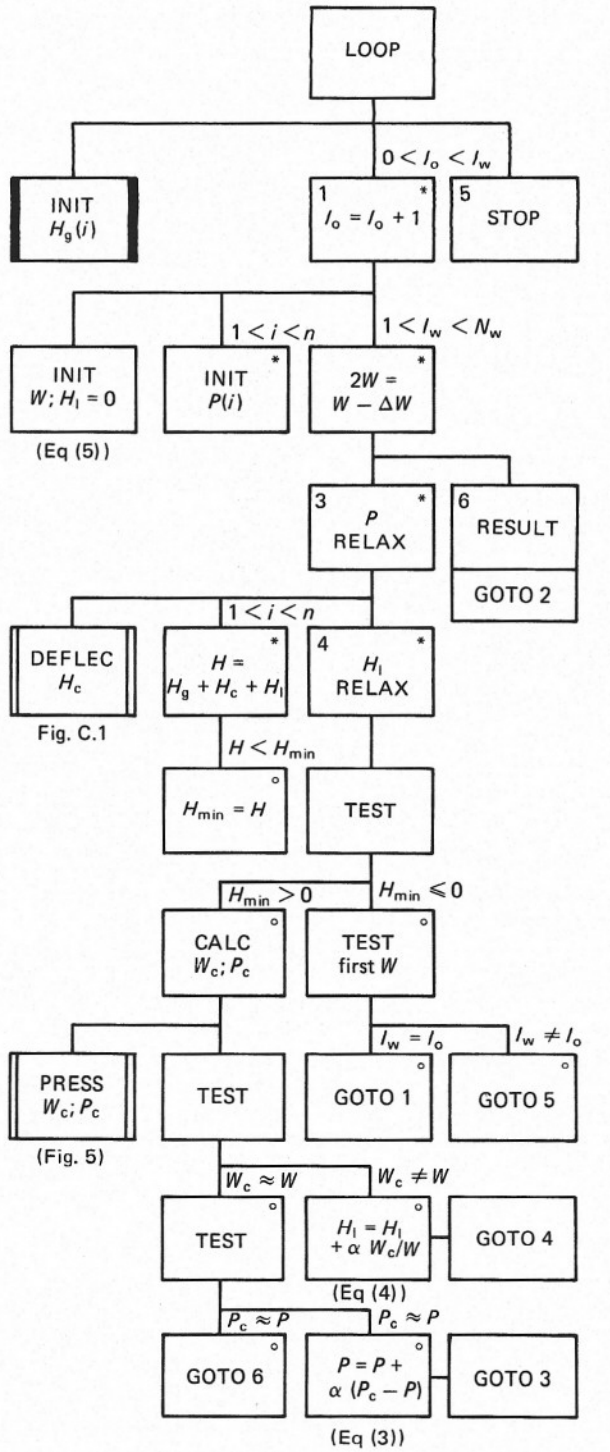

Fig 9 Diagram of the calculation of bearing displacement, H_l, *at prescribed load-carrying capacities,* W

Normally, the load capacity is calculated for a given gap height. This method gives problems for a bearing with negative stiffness. As one can see in Fig 2 two different loads are possible at the same gap height. We found that our program always iterates to the highest load capacity even if the initial guess for the pressure distribution is in the neighbourhood of the other solution. Therefore, it is important to look for a procedure where the gap height can be found from a prescribed load capacity. First we discuss the normal procedure.

Load capacity for a prescribed gap height

The calculation method is illustrated in Fig 8. The layout of this figure is adapted to facilitate comparison with Fig 9.

The iteration starts with an initial guess for the pressures at the nodes. From this estimation of the pressure distribution the nodal deflections $H_c\,(1, \ldots, n)$ of the membrane are calculated (in subroutine DEFLEC). In the array $H_g\,(1, \ldots, n)$ the gap geometry as obtained by the grinding process plus the deflection from the supply pressure in the chamber and ambient pressure in the gap are stored. Hereafter, the gap heights at all nodes can be determined by adding $H_c\,(1, \ldots, n)$ and $H_g\,(1, \ldots, n)$ to the bearing displacement, H_l. Simultaneously, the minimum value of the gap height, H_{min}, is derived. Then a test is performed to investigate whether a negative gap height occurs. If so, the execution of the program is stopped. With this gap geometry

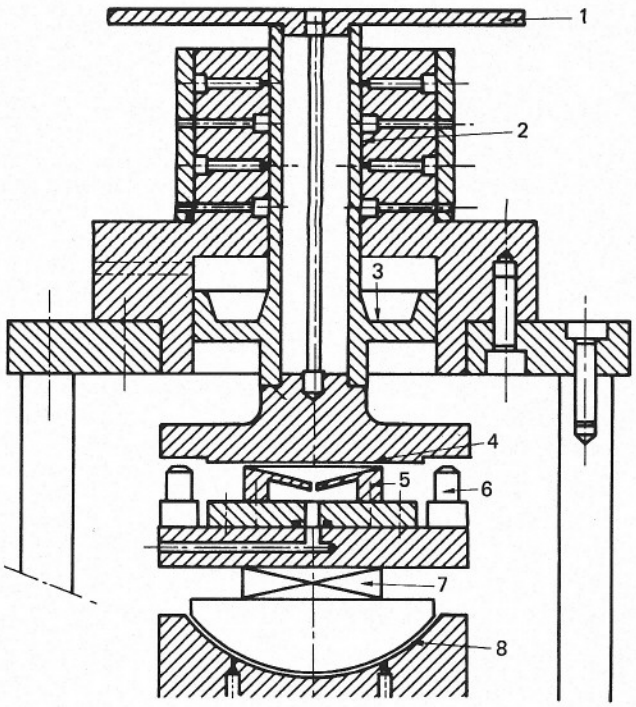

Fig 10 Measurement set-up: 1, load platform for mass loading; 2, air bearing for frictionless guidance; 3, chamber for pressure (vacuum) loading; 4, opposing surface for the bearing to be measured; 5, bearing to be measured; 6, displacement transducers; 7, force transducer; 8, partial spherical bearing for alignment

fixed the pressure distribution, $P_c\,(1, \ldots, n)$, can be calculated with subroutine PRESS that also calculates the load-carrying capacity, W_c. Further on, the calculated pressure distribution is compared with the initial guessed distribution $P\,(1, \ldots, n)$. From the difference between these pressures a new estimation of the pressure distribution $P\,(1, \ldots, n)$ can be made. This estimation is made by relaxation of the pressure, in equation form:

$$P\,(i) = P\,(i) + a\,\{P_c\,(i) - P\,(i)\} \qquad (3)$$

where i is nodal point number and a is relaxation factor.

The iteration is continued until the pressures are in agreement. The whole action is repeated N_h times for different values of H_1, the actual displacement of the bearing pad.

Gap height for a prescribed load capacity

The calculation method is outlined in Fig 9.

This iteration process also starts with an initial guess of the pressure distribution $P\,(1, \ldots, n)$. The calculated deflection $H_c\,(1, \ldots, n)$ increased with $H_g\,(1, \ldots, n)$ gives the shape of the gap. The aim now is to find a displacement, H_1, so that the calculated load capacity W_c corresponds with the prescribed load capacity W. The pressure calculations are carried out with an estimated H_1 followed by a test of the load capacity. If the calculated load capacity is higher than the desired load capacity the calculation is repeated with an increased value for H_1. In the other case the value for H_1 is decreased. This is also a kind of relaxation, governed by

$$H_1 = H_1 + \Delta H\,(W_c - W)/W \qquad (4)$$

This procedure is continued until W_c corresponds with W. If this criterion is satisfied then the differences between the pressures $P_c\,(1, \ldots, n)$ and $P\,(1, \ldots, n)$ are checked in the same way as described above.

An additional difficulty arises as to how high a load capacity is possible for the bearing pad under consideration. The ultimate maximum load-carrying capacity, W_{max}, is given by

$$W_{max} = \pi R\,(n)^2\,(P_s - P_a)$$

Now we start at a prescribed $W = W_{max} - \Delta W$ and check whether a negative gap height occurs. If so, we decrease W with ΔW and repeat the attempt to find a solution. After the first solution is found, it is no longer true that $I_o = I_w$ and the actual calculation can start. If a negative gap height occurs again then the computing has to be stopped because then we have arrived near to point d from figure 2.

As one can see in Fig 9 the procedure is almost the same as that in Fig 8, except that two extra loops are introduced.

Experiments

Load–displacement measurements

With the apparatus schematically shown in Fig 10 it is possible to measure the load–displacement characteristic. The apparatus consists of an axis (1) with externally pressurized bearings (2). By means of the pressure chamber (3) an external load can be applied to the bearing pad. This load is measured with a Kistler piezoelectric force transducer (7). The signal from the transducer is fed to a charge amplifier which can be used for static and dynamic measurements as well. For the dynamic measurements this apparatus has the nice feature that mass and external load can be varied independently. The experiments discussed in this report are all steady-state measurements. Because one can connect the pressure chamber (3) to a vacuum, even zero load is possible to achieve.

The air gap is measured by two inductive displacement transducers (6). To be able to position both bearing surfaces parallel to each other a partial spherical air bearing (8) is used. The positioning can be done by pushing the opposing surfaces against each other with pressurized air supplied to the spherical bearing. Afterwards that air supply is changed over to a vacuum connection to fix the parallel adjustment.

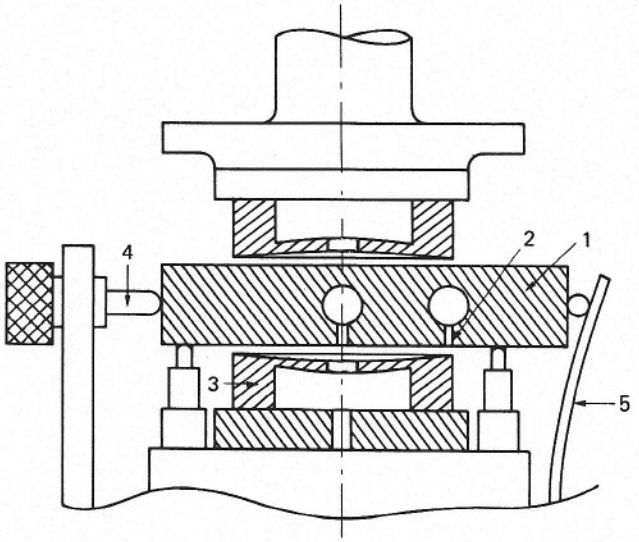

Fig 11 Modified measurement set-up for pressure distribution: a plate (1) with two holes (2) that are connected to pressure gauges can be displaced over the bearing pad to be measured (3); that displacement is monitored by a micron spindle (4) prestressed by a leaf spring (5) that also prevents rotation

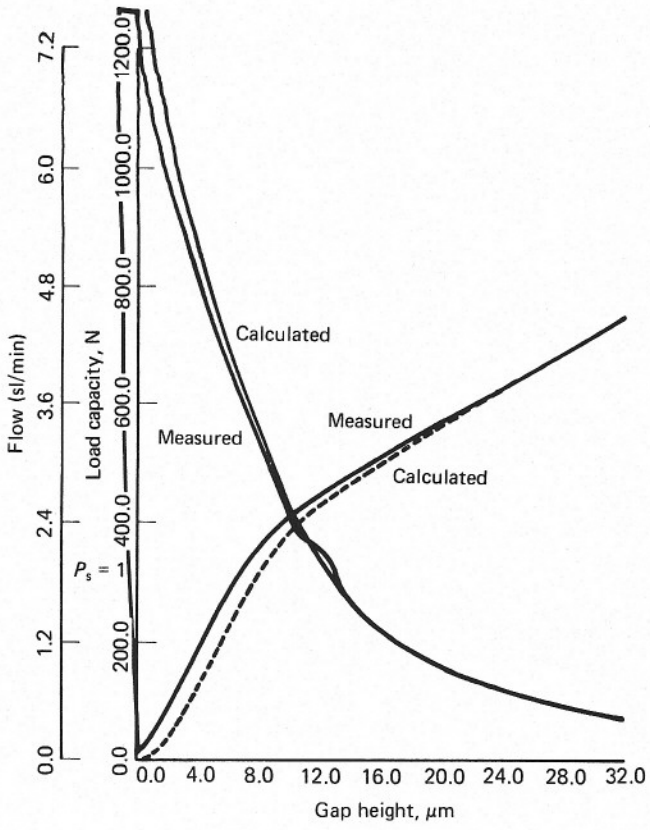

Fig 12 Calculated and measured values of load and flow for a circular rigid bearing pad with a conical gap (D_d = 60 mm, D_t = 0.53 mm, T_t = 13 μm, P_s = 6 bar)

The signals coming from the charge amplifier and displacement transducers are connected to an X–Y recorder, so that the load displacement characteristic can be recorded continuously.

Flow measurements

The flow measurements are carried out with a Tylan mass-flow meter. These flow meters are supplied in a number of standard flow ranges. We used two flow meters with ranges of 0.02–1 sl/min and 0.15–5 sl/min.

The method of operation is based on the fact that the temperature rise of a gas is a function of the amount of heat added, the mass-flow rate and gas properties. The amount of heat is measured and transformed to a linear output signal of 0–5 V dc over the selected flow range.

The response is rather slow (more than 6 s), so the flow measurements must be taken step by step, and no continuous recording is possible.

Pressure distribution measurements

To measure the pressure distribution we modified the measuring set-up of Fig 10 to that of Fig 11. The basic idea was to measure the pressure via a little hole (connected to a pressure gauge), that can radially displace over the bearing pad to be investigated.

To halve the stroke we used two holes drilled into the plate, the outer radius apart. The plate can be displaced by a microspindle prestressed by a leafspring. As one sees from Fig 11 the plate moves between two air bearing pads, the lower one of them to be measured.

Comparison of calculation and experiments

Bearing with a rigid non-parallel gap shape

These bearings are measured because they reveal valuable data (discharge coefficients C_{do} and C_{di}) for the compliant bearings. Figs 12 and 13 give measured and calculated data for pure conical bearing pads.

From the flow curve of Fig 12 we detect the discharge coefficients. The C_{do} value is chosen to fit the slope of the measured curves at very large gap heights. Then the C_{di} value is determined for a good fit of the entire curve. We learned that great care must be spent in making the holes, due to flash, out-of-roundness and tapering. The load curve for p_s = 1 bar indicates the rigidity of the measuring set-up. For gap heights between 10 and 14 μm we observed pneumatic hammer as can be seen from the irregularities in the load curve of Fig 12. This pneumatic hammer is due to the excessive bevelling of 13 μm for this diameter of 60 mm bearing pad.

Bearing with a pivoting membrane

The gap height for these experiments is zeroed by forcing the membrane flat by applying a high enough external load (see Fig 1(c)). For the calculations the gap height is defined as the film thickness under the pivot, so there is no discrepancy in gap height between measurement and calculation. Please notice that the gap height defined thus is (sometimes much) larger than the minimum film thickness in the bearing gap.

In Fig 14 the measurements and calculations for a bearing with an outer diameter of 60 mm are shown. With a shift of 2 μm in gap height we find very good agreement. Such a shift can be expected from manufacturing inaccuracy (flatness and roughness).

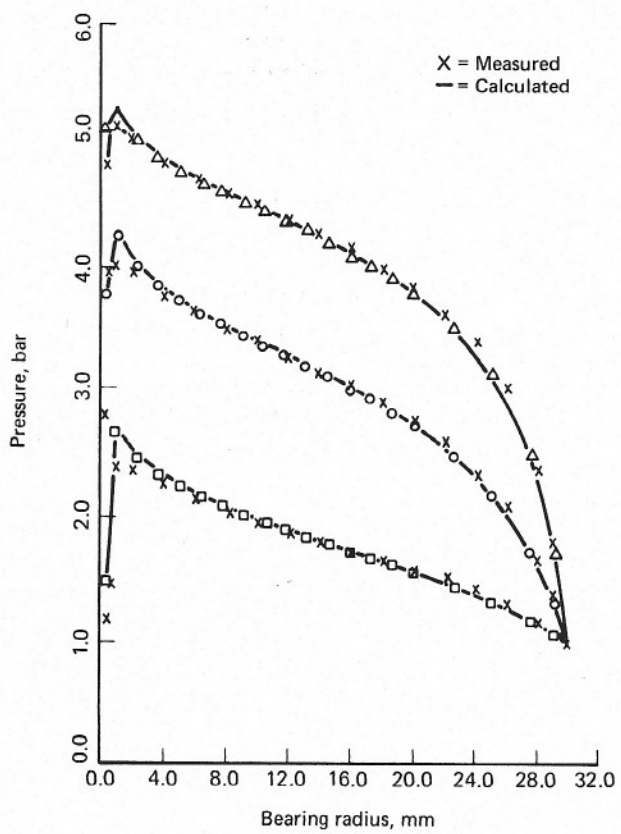

Fig 13 Calculated and measured values of pressure distribution at different gap heights for the bearing pad of Fig 12

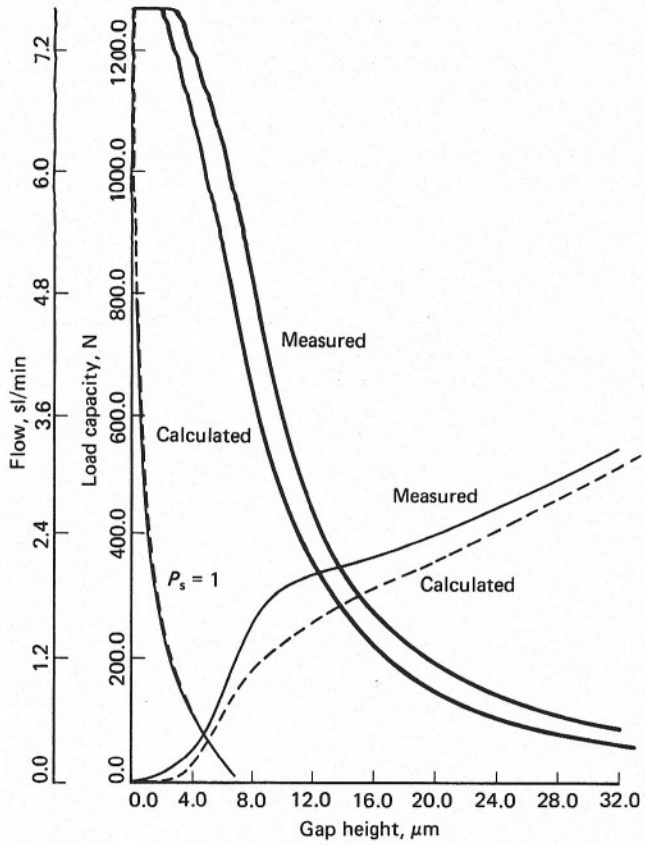

Fig 14 Calculated and measured values of load and flow characteristics for a circular bearing pad with a pivoting membrane and 60 mm outer diameter (D_n = 60 mm, D_t = 0.51 mm, D_s = 45.8 mm, H_i = 2.3 mm, H_o = 1.8 mm, P_{si} = 5.5 bar, T_t = 0, P_s = 6 bar)

In this case the load curve for p_s = 1 bar also shows the deflection of the outer part of the membrane. Although infinite stiffness does not occur at a supply pressure of 6 bar, one sees a definite gain in stiffness.

We designed a bearing pad with 35 mm outer diameter for infinite stiffness at a supply pressure of 6 bar. The resulting characteristics of that design are shown in Fig 15. The measured data are in good agreement with the calculated ones.

Bearing with clamped inner membrane

For this bearing the gap height is the same for measurements as for calculations, namely the film thickness at the outer diameter. Kilmister shows two experimentally derived curves in Ref 2. In Fig 16 one curve is compared with our calculated curves. As one can see, there is good agreement.

Conclusions

The analysis presented in this paper is used as a basis for a computer program to be used by designers. Comparison of the calculation with experiments shows very good agreement.

The program proved that it is possible to design a bearing pad with pivoting membrane on demand. Several attempts by an experienced designer to perform the same job by trial and error have failed before. Further development on circular bearing pads will be focused on the theoretical analysis of pneumatic hammer instability. For such a dynamic analysis an accurate estimation of the static equilibrium, as achieved here, is a starting condition.

References

1. **Kilmister, G.T.F.** A self-compensation flow restrictor for externally pressurized bearings. *Gas Bearing Symposium, Southampton, March 1971, paper 17*
2. **Rowe, W.B. and Kilmister, G.T.F.** A theoretical and experimental investigation of a self-compensating externally pressurized thrust bearing. *Gas Bearing Symposium, Southampton, March 1974, paper D1*
3. **Blondeel, E., Snoeys, R. and Devrieze, L.** Externally pressurized bearings with variable gap geometries. *Gas Bearing Symposium, Cambridge, July 1976, paper E2*
4. **Hayashi, K.** Investigation on externally pressurized gas-lubricated, circular thrust bearing with flexible surface. *Gas Bearing Symposium, Leicester, April 1981, paper 1*
5. **Hagen, J.L.M. and Franken, A.J.J.** *European patent specification, number 0065 337*
6. **Zeiss, Firma Carl.** *Europaeische Patentanmeldung, Anmeldenummer 84114563.4, D-7920 Heldenheim (Brenz) (DE), Erfinder: Enderle, E. and Kaufmann, D.*
7. **Jackson, M.A.** *Principles of program design, Academic Press Inc. (London) Ltd, 7th printing, 1983*
8. **McCabe, J.T., Elrod, H.G., Carfagno, S. and Colsher, R.** Summary of investigations of entrance effects of circular gas bearings. *Gas Bearing Symposium, Southampton, April 1969*
9. **Kamel, H.A. and Osgood, R.M.** *GIFTS primer; a first introduction to the GIFTS-5 system, College of Engineering, University of Arizona, Tucson, AZ, 1979*
10. **Timoshenko, S. and Woinowsky-Krieger, S.** *Theory of plates and shells, McGraw-Hill, 2nd edn, 1959*

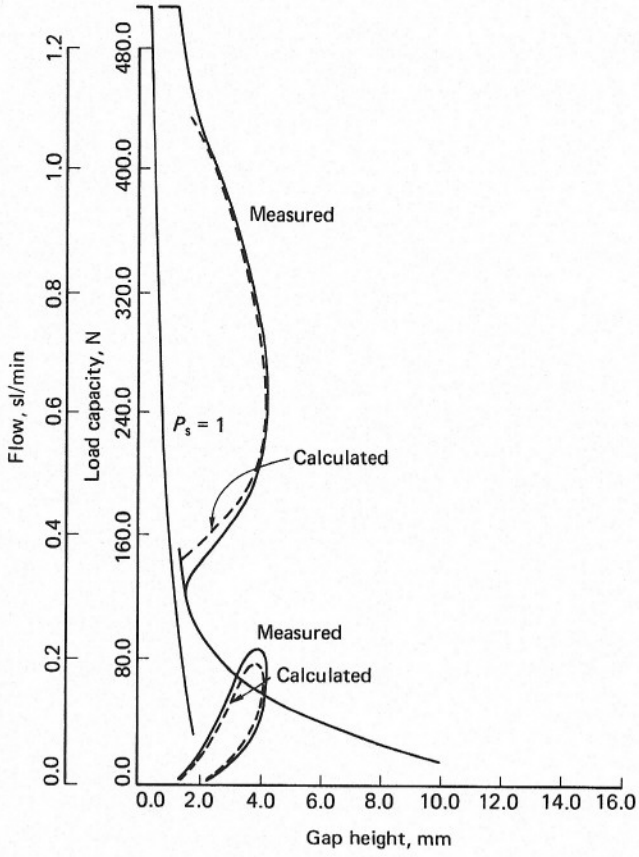

Fig 15 Calculated and measured values of load and flow characteristics of a circular bearing pad with a pivoting membrane and 35 mm outer diameter (D_n = 35 mm, D_t = 0.5 mm, D_s = 31 mm, H_i = 1.25 mm, H_o = 0.75 mm, P_{si} = 3.5 bar, T_t = 0, P_s = 6 bar)

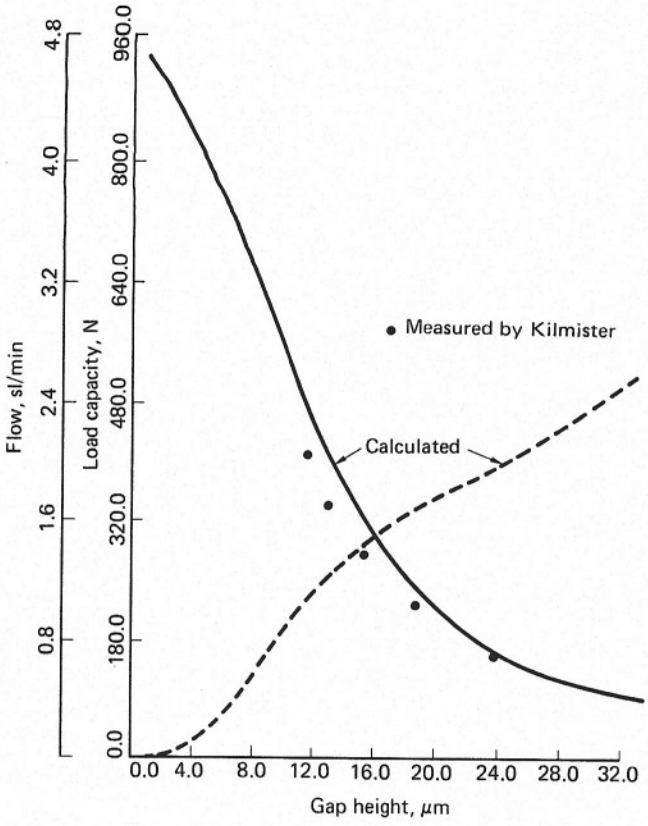

Fig 16 Comparison of our calculations with Kilmister's experimental data for a circular bearing pad with a clamped membrane (D_n = 76.2 mm, D_t = 0.51 mm, D_s = 25.4 mm, H_i = 0.79 mm, P_{si} = 1 bar, T_t = 11.43 μm, P_s = 5.14 bar)

Appendix A: Radial gas flow in a non-parallel bearing gap

The isothermal Navier–Stokes equations of motion in cylindrical coordinates (R, θ, Z) reduce to

$$\frac{dP}{dR} = \eta \frac{d^2U}{dZ^2}$$
$$\frac{dP}{dZ} = 0 \qquad \text{(A1)}$$
$$\frac{dP}{d\theta} = 0$$

Herein U is the radial velocity, η the dynamic viscosity and P the pressure. We used $dU/dR \ll dU/dZ$; the inertial forces are neglected, and owing to axisymmetry all circumferential effects cancel.

Solving these equations and inserting the boundary conditions ($U = 0$ at $Z = 0$ and at $Z = H$) yields

$$U = \frac{Z(Z-H)\,dP/dR}{2\eta} \qquad \text{(A2)}$$

So the mass flow becomes

$$M_{gap} = \rho\, 2\pi R \int_0^H U\, dZ = -(\pi R \rho H^3/6\eta)\frac{dP}{dR} \qquad \text{(A3)}$$

For compressible isothermal flow ($P = \rho R_g T$) and constant viscosity, integration of this equation gives

$$dP^2 = -(12\eta R_g T/\pi) M_{gap} \frac{dR}{R H^3} \qquad \text{(A4)}$$

For a linear gap between two nodes R_b and R_e with corresponding nodal gap heights H_b and H_e one can write

$$H = A + B R \qquad \text{(A5a)}$$

with

$$A = \frac{H_b R_e - H_e R_b}{R_e - R_b} \qquad \text{(A5b)}$$

$$B = \frac{H_e - H_b}{R_e - R_b} \qquad \text{(A5c)}$$

Substituting Eq (A5a) into (A4) gives an equation that can be integrated analytically to find

$$P^2 = -(12\eta R_g T/\pi) M_{gap}\, Fun\,(A, B, R) + C \qquad \text{(A6)}$$

with

$$Fun\,(A, B, R) = \int dR/(R H^3)$$
$$= \frac{\{(A+H)/H\}^2/2 + \log(R/H)}{A^3} \qquad \text{(A7)}$$

In the specific case that $A = 0$, this simplifies to

$$Fun\,(0, B, R) = \frac{-1}{3(BR)^3} \qquad \text{(A8)}$$

Suppose we have divided the radius into $n - 1$ segments with n nodes; then for segment i we get: $R_b = R(i)$, $R_e = R(i+1)$, $P_b = P(i)$, $P_e = P(i+1)$ and $A = A(i)$, $B = B(i)$, so we can write

$$P^2(i) - P^2(i+1) = (12\eta R_g T/\pi) M_{gap}\, Int(i) \qquad \text{(A9)}$$

with

$$Int(i) = Fun\,\{A(i), B(i), R(i+1)\}$$
$$- Fun\,\{A(i), B(i), R(i)\} \qquad \text{(A10)}$$

For the total gap we know that $P(1) = P_{in}$, the pressure at the entrance of the gap, and that $P(n) = P_a$, the ambient pressure. By adding all equations (A9) we arrive at

$$P_{in}^2 - P_a^2 = (12\eta R_g T/\pi) M_{gap} \sum_{i=1}^{n-1} Int(i) \qquad \text{(A11)}$$

with

$$Som = \sum_{i-1}^{n-1} Int(i)$$

we can rewrite Eq (A11):

$$M_{gap} = \frac{P_{in}^2 - P_a^2}{12\eta R_g T\, Som/\pi} \qquad \text{(A12)}$$

The procedure outlined above can easily be applied in numerical computation, as will be evident from Fig 17.

Appendix B: Gas flow through an inlet restrictor

The inlet restrictor is considered to be composed of two apertures arranged in series. With an inlet hole of diameter $2R(1)$ we have

$$A_{or} = \pi R(1)^2 \qquad \text{(B1a)}$$

$$A_{in} = 2\pi R(1) H(1) \qquad \text{(B1b)}$$

In Fig 4 one can see the schematic pressure drops occurring in the inlet restrictor. Across the orifice aperture, A_{or}, the pressure drops from supply pressure, P_s to an intermediate

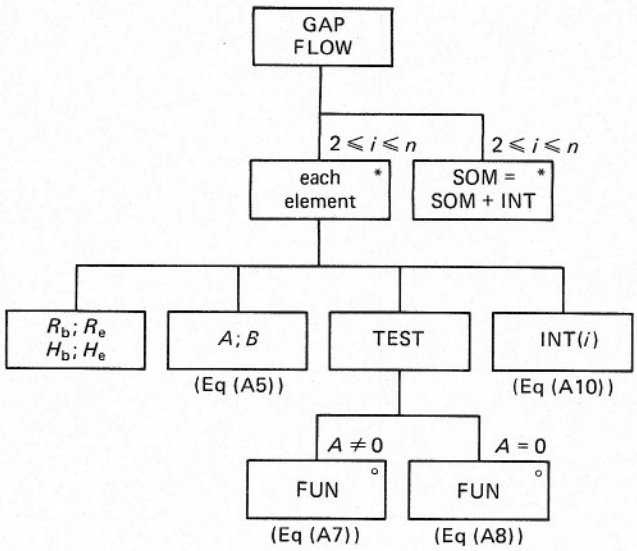

Fig 17 Diagram of gap flow calculations

pressure, P_{or}. Across the inherent aperture, A_{in}, there is theoretically a further pressure drop to P_{th}, but owing to a pressure recovery the pressure rises thereafter to P_{in}. That pressure P_{in} is considered to be the effective pressure at the entrance of the bearing gap.

The mass flow through both apertures is governed by the compressible Bernouilli equation. For a pressure drop from P_b to P_e across an aperture with area A, one can write

$$M = C\,P_b\,F_m\,(P_e/P_b) \tag{B2}$$

with

$$C = C_d\,A\,\sqrt{\{2k/(k-1)\,R_g\,T\}} \tag{B3}$$

For C we distinguish between C_{in}, with $C_d = C_{di}$ and $A = A_i$, and C_{or} with $C_d = C_{do}$ and $A = A_o$. The function F_m depends on the flow regime. For choked flow, if

$$P_e/P_b \leqslant \{2/(k+1)\}^{k/(k-1)} \tag{B4}$$

then

$$F_m\,(P_e/P_b) = F_{mkr} = [\{2/(k+1)\}^{1/(k-1)}]\,\sqrt{\{(k-1)/(k+1)\}} \tag{B5}$$

else

$$F_m\,(P_e/P_b) = \sqrt{(P_e/P_b)^{2/k} - (P_e/P_b)^{(k+1)/k}} \tag{B6}$$

Where k is the coefficient of adiabatic expansion.

The pressure recovery is determined by the K factor, which is defined by

$$K = (P_{or} - P_{in})/(P_{or} - P_{th}) \tag{B7}$$

From McCabe, Elrod and others[8] we know the empirical relationship

$$K = 0.2 + 0.5\,(1 - e^{-Re/1200})^2 \tag{B8}$$

The Reynolds number, Re, can be calculated from the mass flow through the inherent aperture (with hydraulic diameter D_h):

$$Re = \rho\,U_{gem}\,D_h/\eta = (M_{in}/A_{in})\,2H\,(1)/\eta = M_{in}/(\pi\,R\,(1)\,\eta) \tag{B9}$$

For the mass flow through the bearing gap, Eq (A12) gives

$$M_{gap} = C_{gap}\,(P_{in}^2 - P_a^2) \tag{B10}$$

with

$$C_{gap} = \pi/(12\eta\,R_g\,T\,Som) \tag{B11}$$

Because we want to calculate P_{in} at a pre-determined gap shape the quantity Som in Eq (B11) is known (see Appendix A).

The formulae given above are sufficient to determine the unknowns P_{or}, P_{in}, P_{th} and M. But unfortunately most formulae are in implicit form. Therefore, we define two functions from which the zeros must be located:

$$F_1\,(P_{or}) = M_{gap} - M_{in} \tag{B12}$$

$$F_2\,(P_{in}) = M_{gap} - M_{or} \tag{B13}$$

Our program uses a NAG subroutine CO5ADF to locate the zero of function F_2. Within that function F_2, another subroutine, REGFAL (using the regula falsi method) locates the zero of function F_1. In Figs 18 to 20 the procedures are drawn in M. Jackson diagrams.

For the function F_2, P_{in} has a known value, estimated by CO5ADF, in the range $P_a < P_{in} < P_s$. So one can calculate M_{gap} (Eq (B10)) and from that Re (Eq (B9)). Then the K factor can be calculated (Eq (B8)), but to prevent underflow the K factor is set to 0.7 if $Re > 10\,000$. Before we can continue we must first determine the value of P_{or} in the region $P_{in} < P_{or} < P_{ormax}$, with subroutine REGFAL. The P_{ormax} follows from choked flow through the inherent aperture, A_{in} (Eq (B1b)). From Eqs (B2) and (B5) we find

$$P_{ormax} = M_{gap}/(C_{in}\,F_{mkr}) \tag{B14}$$

The subroutine REGFAL estimates P_{or} and uses F_1 to test that estimation. Within F_1 the known value of P_{or} is used to calculate P_{th} from the K factor (Eq (B7)). To prevent unrealistic calculation one should ensure that $P_{th} \geqslant 0$. Then one can calculate M_{in} (Eqs (B2) and (B5) or (B6) with $P_b = P_{or}$ and $P_e = P_{th}$. In the unrealistic situation during numerical calculation that $P_{or} < P_{th}$ one sets $M_{in} = 0$, by means of $F_m = 0$.

Now the routine REGFAL checks whether M_{in} equals M_{gap} to the desired accuracy. If not it starts again with a better guess of P_{or}. Having found the P_{or} we can continue within the function F_2 to calculate M_{or} (Eqs (B2) and (B5) or (B6) with $P_b = P_s$ and $P_e = P_{or}$). If P_{or} happens to be larger than P_s one sets $M_{or} = 0$, by means of $F_m = 0$ (Eq (B2)). Also the NAG routine checks whether F_2 equals zero within the desired accuracy, and if necessary it restarts with a better guess of P_{in}.

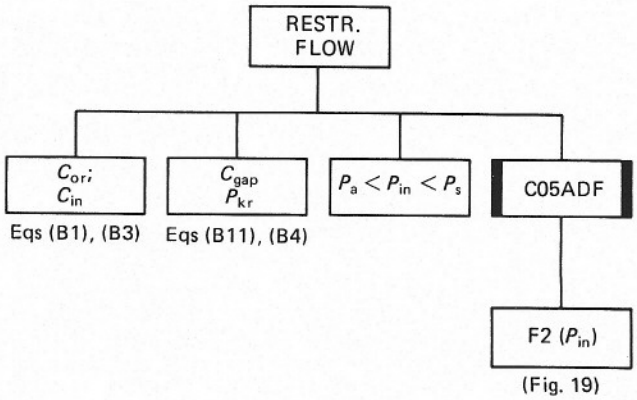

Fig 18 Diagram of flow calculation and pressures in inlet restrictor

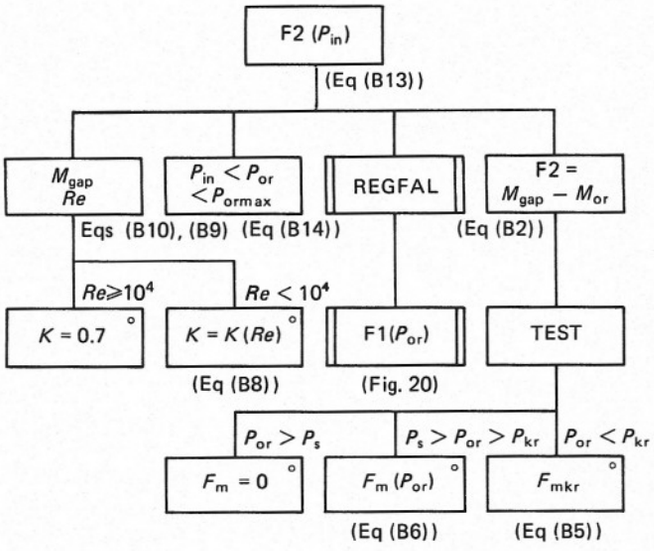

Fig 19 Diagram of help-function F_2 *used to equate gap flow and orifice flow*

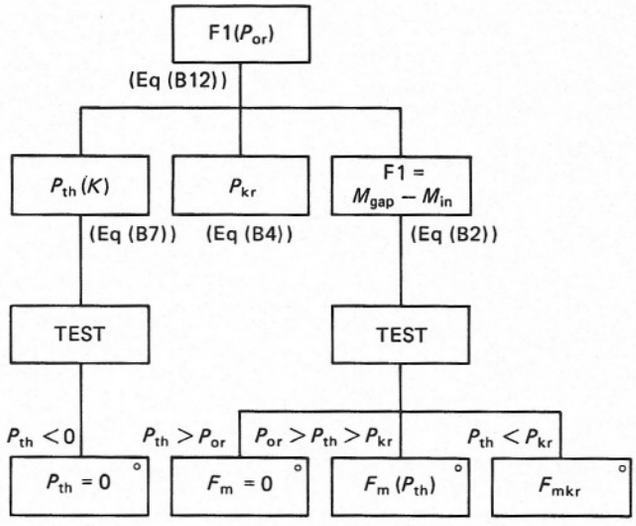

Fig 20 Diagram of help-function F_1 *used to equate gap flow and flow through inherent aperture*

At the end of those iterations the unknowns P_{or}, P_{th}, P_{in} and M_{gap} are evaluated.

Appendix C: Deflection of circular plates

A circular plate loaded with a shearing force (per unit length) S and with flexural rigidity D leads to the following differential equation for the deflection Y as can be found in the book by Timoshenko[10]:

$$\{(R\,Y')'/R\}' = S/D \tag{C1}$$

$$M_r = -D\,(Y'' + Y'\,\nu/R) \tag{C2}$$

$$M_t = -D\,(Y'/R + \nu\,Y'') \tag{C3}$$

with

$$D = \frac{E\,H^3}{12\,(1-\nu^2)} \tag{C4}$$

Herein E is the modulus of elasticity, ν is Poisson's ratio, and H is the thickness of the plate under consideration. The bending moments per unit length M_r and M_t act along circumferential sections and diametrical sections of the plate, respectively.

The magnitude of the shearing force at a distance from the centre of a membrane can be derived from

$$S\,R = {}_0\!\int^R P\,R\,\mathrm{d}R \tag{C5}$$

The pressure distribution acting upon the membrane can be approximated by nodal pressures with linear interpolation between the nodes. This is the same approximation as used in Appendix A, when calculating the gap flow. For each specific segment extending from radius R_b up to radius R_e the pressure can be expressed by

$$P = P_0 + Q\,R \tag{C6}$$

The deflection due to this pressure acting on that specific segment is calculated from, firstly, loading the membrane with that pressure up to $R = R_e$ and, secondly, loading it with the opposite pressure up to $R = R_b$. As can be seen in the M. Jackson diagram of Fig 22 this leads to repeating the same calculation several times. That calculation is elaborated below.

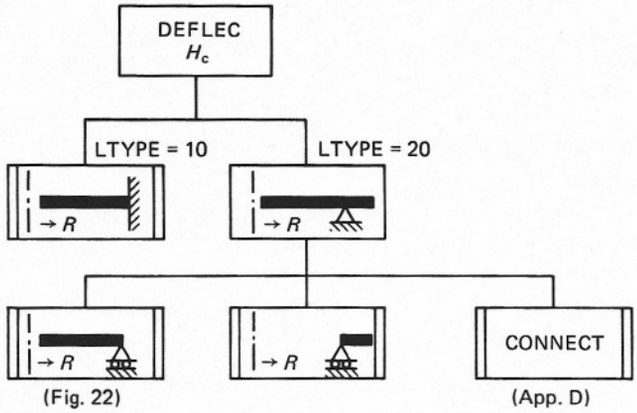

Fig 21 Diagram of the calculation of the membrane deflections. Ltype = 10 indicates a clamped inner membrane and Ltype = 20 a pivoting membrane

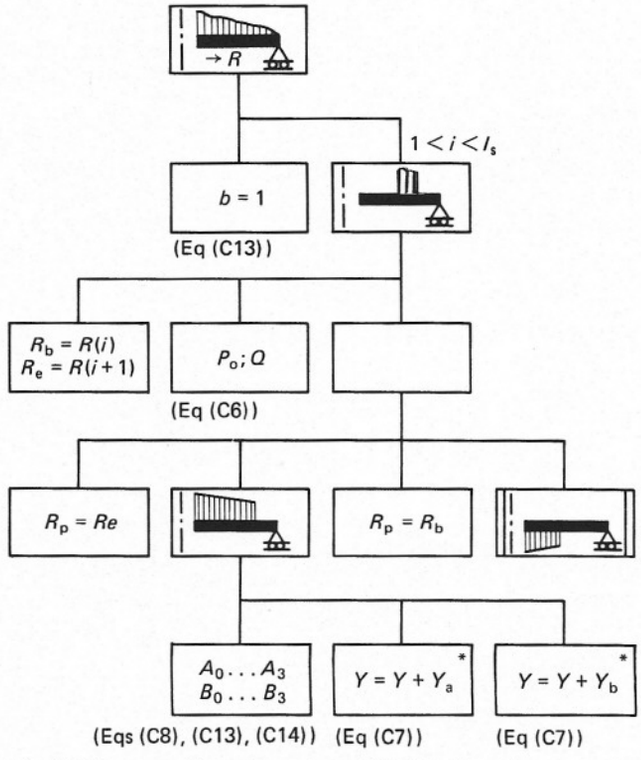

Fig 22 Diagram of a subroutine of Fig 21 that illustrates the calculation of the deflection of a pivoted inner membrane

If R_p is the radius up to which a pressure (given by Eq (C6)) acts we bisect the membrane into sections a (with $R < R_p$) and b (with $R > R_p$), with different equations for their shearing forces (S_a and S_b, respectively) because Eq (C5) yields

$$S_a R = \int_{R(1)}^{R} (P_0 + Q R) R \, dR$$

and

$$S_b R = \int_{R(1)}^{R_p} (P_0 + Q R) R \, dR$$

Solving Eq (C1) yields

$$\begin{aligned} D Y_a &= Q R^5/225 + P_0 R^4/64 - A_0 R^2 \log (R/R_s) + \\ &+ A_2 \log (R/R_s) + A_3 + A_1 R^2 \\ D Y_b &= - B_0 R^2 \log (R/R_s) + B_1 R^2 + B_2 \log (R/R_s) \\ &+ B_3 \end{aligned} \quad \text{(C7)}$$

We introduced the radius R_s at which boundary conditions are known; these are introduced below (Eqs (C13) or (C16)). The above values of S_a and S_b give

$$A_0 = \frac{Q R (1)^3}{12} + \frac{P_0 R (1)^2}{8} \quad \text{(C8a)}$$

and

$$B_0 = \frac{Q (R (1)^3 - R_p^3)}{12} + \frac{P_0 (R (1)^2 - R_p^2)}{8} \quad \text{(C8b)}$$

This leaves us with six unknown constants A_1, A_2, A_3, B_1, B_2 and B_3. To solve these constants, we first use the fact that at radius $R = R_p$ both sections must connect smoothly, so we write

$$\begin{aligned} Y_a (R_p) &= Y_b (R_p) \\ Y_a' (R_p) &= Y_b' (R_p) \\ Y_a'' (R_p) &= Y_b'' (R_p) \end{aligned} \quad \text{(C9)}$$

The third condition also ensures equal moments at $R = R_p$. Now we can deduce the following three equations for the six unknowns:

$$B_1 - A_1 = (B_0 - A_0) \{1 + \log (R_p/R_s)\} + \frac{Q R_p^3}{36} + \frac{P_0 R_p^2}{16} \quad \text{(C10)}$$

$$A_2 - B_2 = (B_0 - A_0) R_p^2 + \frac{Q R_p^5}{30} + \frac{P_0 R_p^4}{16} \quad \text{(C11)}$$

$$\begin{aligned} A_3 - B_3 &= (B_0 - A_0) R_p^2 \\ &\frac{\{1 - \log (R_p/R_s) + Q R_p^5 (0.7 - \log (R_p/R_s)\}}{30} \\ &+ \frac{P_0 R_p^4 \{3/4 - \log (R_p/R_s)\}}{16} \end{aligned} \quad \text{(C12)}$$

The remaining three equations needed to solve the constants follow from the particular membrane under consideration. The clamped membrane gives very simple conditions but the pivoting membrane is too complicated to analyse directly. Therefore, we bisect that membrane at the pivot radius and restrict the analysis for the moment to simple inner and outer membranes (see Fig 21). Appendix D shows how both sections can be connected together.

That leaves us for the moment with the situations that are summarized in Fig 23, from which the appropriate boundary conditions can be selected.

For the inner membrane one can find (Fig 23 and Eq (C2)):

$$Y_b (R_s) = 0 \quad \text{(C13a)}$$

$$b \, Y_b'' (R_s) + \nu \, Y_b' (R_s)/R_s = 0 \quad \text{(C13b)}$$

$$R (1) \, Y_a'' (R (1)) + \nu \, Y_a' (R (1)) = 0 \quad \text{(C13c)}$$

For D we write

$$D_i = E H_i/12 (1 - \nu^2) \quad \text{(C13d)}$$

The b indicates whether the membrane is clamped ($b = 0$) or pivoted ($b = 1$) at radius R_s.

Now we can derive the other three equations, valid only for the inner membrane, to find

$$B_3 = - B_1 R_s^2 \quad \text{(C14a)}$$

$$B_1 = \frac{(3b + \nu) B_0}{2 (b + \nu)} + \frac{(b - \nu) B_2}{2 R_s^2 (b + \nu)} \quad \text{(C14b)}$$

$$\begin{aligned} A_2 &= \frac{(4 + \nu) Q R (1)^5}{45 (1 - \nu)} \\ &+ \frac{(3 + \nu) \{P_0 R (1)^4/16 - A_0 R (1)^2\}}{1 - \nu} \\ &+ (1 + \nu) 2R (1)^2 \frac{\{A_1 - A_0 \log (R (1)/R_s)\}}{1 - \nu} \end{aligned} \quad \text{(C14c)}$$

In the specific case $R (1) = 0$ then

$$A_2 = 0 \quad \text{(C14d)}$$

This terminates the derivation of the constants for an inner membrane, because the remaining part is straightforward. Having found the constants of integration one can use Eq (C7) to calculate the deflections.

For the outer membrane a similar reasoning leads to different formulae for the constants of integration. We also bisect the outer membrane into section a ($R < R_p$) and section b ($R > R_p$). The shearing forces become:

$$S_a R = -\int_{R_s}^{R_p} (P_0 + Q R) R \, dR + \int_{R_s}^{R} (P_0 + Q R) R \, dR$$

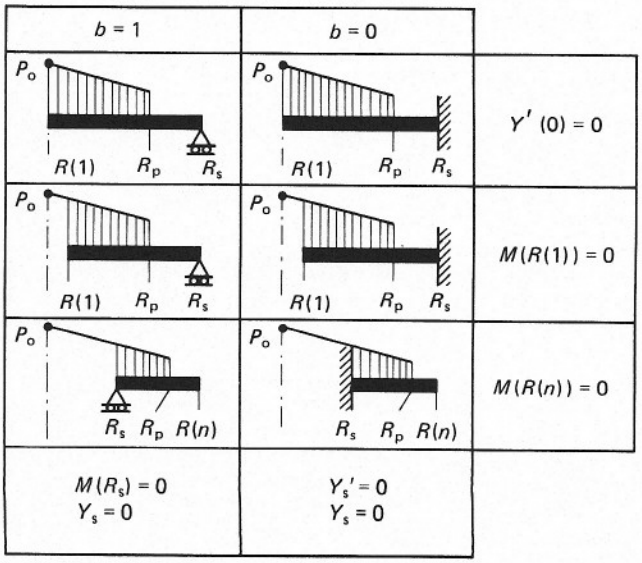

Fig 23 Boundary conditions valid for the various types of circular membrane

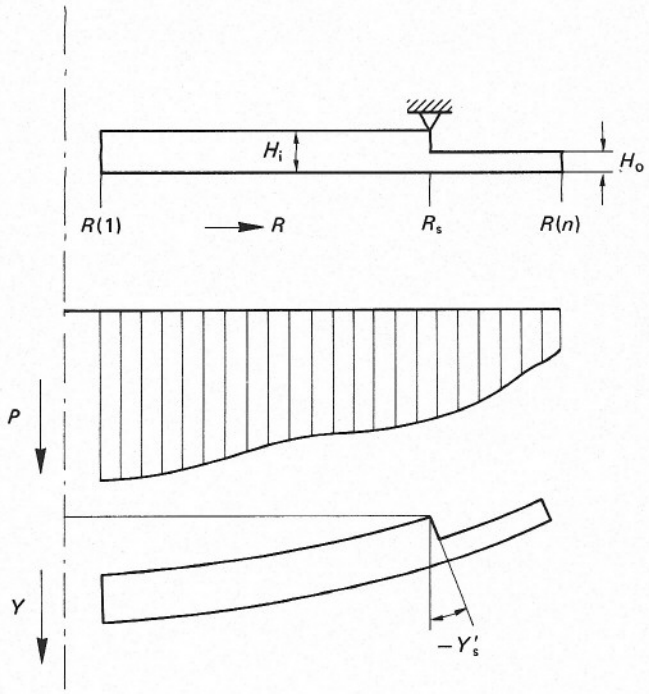

Fig 24 Dimensions, loading and deflection of a pivoting membrane

and

$$S_b = 0$$

This gives the same Eq (C7) but now

$$A_0 = \frac{Q R_p^3}{12} + \frac{P_0 R_p^2}{8} \text{ and } B_0 = 0 \qquad \text{(C15)}$$

Eqs (C10), (C11) and (C12) still hold.

Using the boundary conditions of Fig 23 yields

$$Y_a(R_s) = 0 \qquad \text{(C16a)}$$

$$b\,Y_a''(R_s) + \frac{\nu\,Y_a'(R_s)}{R_s} = 0 \qquad \text{(C16b)}$$

$$R(n)\,Y_b''(R(n)) + \nu\,Y_b'(R(n)) = 0 \qquad \text{(C16c)}$$

For D we write

$$D_o = \frac{E H_o}{12(1-\nu^2)} \qquad \text{(C16d)}$$

And after some elaboration one finds

$$A_3 + A_1 R_s^2 = \frac{-Q R_s^5}{225} - \frac{P_0 R_s^4}{64} \qquad \text{(C17a)}$$

$$B_1 = \frac{(1-\nu) B_2}{2 R(n)^2 (1+\nu)} \qquad \text{(C17b)}$$

$$A_2 = \frac{(4b+\nu) Q R_s^5}{45 (b-\nu)} + \frac{(3b+\nu)(P_0 R_s^4/16 - A_0 R_s^2)}{b-\nu} + \frac{(b+\nu) 2 R_s^2 A_1}{b-\nu} \qquad \text{(C17c)}$$

This completes the analysis of the circular plates as far as needed for the deflection of simple membranes by pressure loading only. It will be clear that, as well as deflections, also their derivatives and the bending moments can be calculated. The complex pivoting membrane is analysed further in Appendix D, using the results found above.

Appendix D: Connecting of inner and outer membranes

The situation to be analysed is drawn in Fig 24. The entire membrane consists of an inner part with thickness H_i and an outer part with a different thickness H_o. The pivot prohibits radial displacement at the upper layer of the inner membrane.

When we bisect the membrane at the radius R_s (pivot radius) then we have two membranes as given in Fig 25. Upon the outer one a force (per unit length) N_o and a bending moment (per unit length) M_o act. The same force and bending moment must act upon the inner membrane in opposite direction plus a force N_s originated by the pivot that prevents radial displacement there. One can easily find from the Fig 25 that the total load for the inner membrane amounts to

$$M_i = M_o + \frac{N_s H_i}{2} + \frac{N_o (H_i - H_o)}{2} \qquad \text{(D1)}$$

$$N_i = N_s - N_o \qquad \text{(D2)}$$

The deflection gradient at $R = R_s$, Y_s', must be equal for both the inner membrane and the outer membrane, or:

$$Y_s' = Y_i'(R_s) = Y_o'(R_s) \qquad \text{(D3)}$$

For both parts of the membrane, that deflection gradient is the result of a pressure loading plus the loading by its bending moment, so:

$$Y_i' = Y_i'(M_i) + Y_i'(P) \qquad \text{(D4)}$$

$$Y_o' = Y_o'(M_o) + Y_o'(P) \qquad \text{(D5)}$$

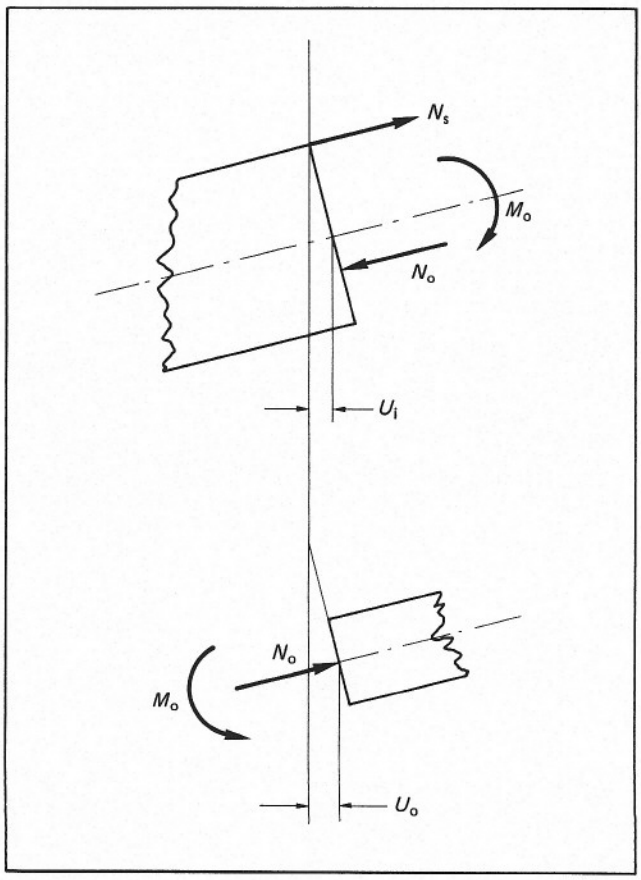

Fig 25 Loading at the interfaces of the bisected parts of the membrane from Fig 24

The $Y'(P)$ is calculated simultaneously with $Y(P)$ with the algorithm as described in Appendix C, and can be regarded as a known quantity at this stage. Because we bisected the membrane at $R = R_s$ we have to distinguish between $Y_{si}'(P)$ and $Y_{so}'(P)$ for the 'known' deflection gradients at $R = R_s$ caused by pressure load only – for inner and outer membrane, respectively.

In the book by Timoshenko[10] one can find the deflection of circular plates loaded by bending moments. At $R = R_s$ we find:

$$Y_{si}'(M_i) = \frac{R_s^2}{R_s^2 - R(1)^2} \left\{ \frac{R_s}{1+\nu} + \frac{R(1)^2}{R_s(1-\nu)} \right\} \frac{M_i}{D_i}$$

or (D6)

$$Y_{si}'(M_i) = C_{mi} M_i$$

$$Y_{so}'(M_o) = \frac{-R_s^2}{R(n)^2 - R_s^2} \left\{ \frac{R_s}{1+\nu} + \frac{R(n)^2}{R_s(1-\nu)} \right\} \frac{M_o}{D_o}$$

or (D7)

$$Y_{so}'(M_o) = -C_{mo} M_o$$

with

$$D_i = \frac{E H_i^3}{12(1-\nu^2)} \quad \text{and} \quad D_o = \frac{E H_o^3}{12(1-\nu^2)} \tag{D8}$$

The forces per unit length N_i and N_o must stretch the membranes in such a way that the displacements in their midplanes at $R = R_s$ coincide with the displacements from the deflection gradient. From Fig 25 one can deduce:

$$U_i = -Y_s' H_i/2 \tag{D9}$$

$$U_o = -Y_s'(H_i - H_o/2) \tag{D10}$$

Timoshenko[10] also gives:

$$U_i = \frac{N_i}{H_i E} \frac{R_s}{R_s^2 - R(1)^2} \{(1-\nu) R_s^2 + (1+\nu) R(1)^2\}$$

or (D11)

$$U_i = C_{ni} N_i$$

$$U_o = \frac{N_o}{H_o E} \frac{R_s}{R_d^2 - R_s^2} \{(1-\nu) R_s^2 + (1+\nu) R_d^2\}$$

or (D12)

$$U_o = C_{no} N_o$$

From Eqs (D6) to (D8), (D11) and (D12) it follows that

$$C_{ni} = \frac{C_{mi} H_i^2}{12} \quad \text{and} \quad C_{no} = \frac{C_{mo} H_o^2}{12} \tag{D13}$$

All equations above lead to the following set of four equations:

$$\begin{bmatrix} 1 & -C_{mi} & -C_{mi} H_i/2 & -C_{mi}(H_i - H_o)/2 \\ H_i/2 & 0 & C_{mi} H_i^2/12 & -C_{mi} H_i^2/12 \\ 1 & C_{mo} & 0 & 0 \\ H_i - H_o/2 & 0 & 0 & C_{mo} H_o^2/12 \end{bmatrix} \begin{pmatrix} Y_s' \\ M_o \\ N_s \\ N_o \end{pmatrix} = \begin{pmatrix} Y_{si}'(P) \\ 0 \\ Y_{so}'(P) \\ 0 \end{pmatrix}$$

This set of equations can easily be solved to give:

$$Y_s' = \frac{C_{mo} Y_{si}'(P) + C_{mi} Y_{so}'(P)}{4 C_{mo} + \{1 + (3 H_i/H_o - 1)^2\} C_{mi}} \tag{D14}$$

$$M_o = \frac{Y_{so}'(P) - Y_s'}{C_{mo}} \tag{D15}$$

$$N_s = \frac{N_o - 6 Y_s'}{H_i C_{mi}} \tag{D16}$$

$$N_o = \frac{-6(2 H_i/H_o - 1) Y_s'}{H_o C_{mo}} \tag{D17}$$

Please notice from equation (D14) that for infinite C_{mo} (no outer membrane) the deflection gradient Y_s' reduces by a factor 4 because of the radially fixed pivot at the upper side of the plate.

From Eq (D1) it follows that

$$M_i = M_o - 3 Y_s' \left\{ \frac{(2 H_i/H_o - 1)^2}{C_{mo}} + \frac{1}{C_{mi}} \right\} \tag{D18}$$

Because $Y_{si}'(P)$ and $Y_{so}'(P)$ are supposed to be known, it is straightforward to calculate the unknown bending moments. The combined deflection can now be calculated from

$$Y = Y(P) + Y(M) \tag{D19}$$

with $Y(P)$ already known from Appendix C and $Y(M)$ following from Timoshenko's formulae[10]:

$$Y_i(M_i) = \frac{-\left\{ \frac{R_s^2}{2} - \left(\frac{1+\nu}{1-\nu} \right) R(1)^2 \log\left(\frac{R}{R_s} \right) - \frac{R^2}{2} \right\} M_i R_s^2}{D_i (1+\nu)(R_s^2 - R(1)^2)}$$

$$Y_o(M_o) = \frac{-\left\{ \frac{R^2}{2} + \left(\frac{1+\nu}{1-\nu} \right) R(n)^2 \log\left(\frac{R}{R_s} \right) - \frac{R_s^2}{2} \right\} M_o R_s^2}{D_o (1+\nu)(R(n)^2 - R_s^2)}$$

It is also possible to calculate the stresses in the membrane, but this is not elaborated here.